

1 **Tropopause Evolution in a Rapidly Intensifying Tropical Cyclone: A Static**
2 **Stability Budget Analysis in an Idealized, Axisymmetric Framework**

3 Patrick Duran* and John Molinari

4 *University at Albany, State University of New York, Albany, NY*

5 **Corresponding author address:* Department of Atmospheric and Environmental Sciences, Univer-
6 sity at Albany, State University of New York, 1400 Washington Avenue, Albany, NY.

7 E-mail: pduran2008@gmail.com

ABSTRACT

8 Large changes in tropopause-layer static stability are observed during the
9 rapid intensification (RI) of an idealized, axisymmetric tropical cyclone (TC).
10 Over the eye, static stability near the tropopause decreases and the cold-point
11 tropopause height rises by up to 4 km at the storm center. Outside of the eye,
12 static stability increases considerably just above the cold-point tropopause,
13 and the tropopause remains near its initial level.

14 A budget analysis reveals that the advection term, which includes differ-
15 ential advection of potential temperature and direct advection of static sta-
16 bility, is important throughout the upper troposphere and lower stratosphere.
17 Within the eye, differential advection plays a particularly important role in
18 destabilizing the layer near and above the cold-point tropopause. Outside of
19 the eye, a radial-vertical circulation develops during RI, with strong outflow
20 below the tropopause and weak inflow above. The upper-tropospheric out-
21 flow layer exports high potential temperature (θ) air from the eyewall to large
22 radii in the upper troposphere. This increase in θ forces stabilization below
23 the outflow jet and destabilization above. Vertical wind shear above and be-
24 low the upper-tropospheric outflow maximum induces vertical gradients of
25 turbulence, which also modify the vertical stability profile. Meanwhile, as or-
26 ganized convection reaches the tropopause, radiative heating tendencies at the
27 top of the cirrus canopy generally act to destabilize the upper troposphere and
28 stabilize the lower stratosphere. Turbulent mixing and radiative heating com-
29 bine to play an important role in the development of the strong stable layer
30 immediately above the cold-point tropopause during RI.

31 1. Introduction

32 Using a high-resolution dropsonde dataset collected during the Tropical Cyclone Intensity ex-
33 periment (TCI; Doyle et al. 2017), Duran and Molinari (2018) observed dramatic changes in
34 tropopause structure during the rapid intensification (RI) of Hurricane Patricia (2015). The goal of
35 the present paper is to analyze the processes that might have produced the upper-tropospheric and
36 lower-stratospheric fluctuations observed in Patricia using an idealized axisymmetric simulation.

37 After undergoing a remarkably rapid intensification (RI), Hurricane Patricia (2015) set a new
38 record as the strongest tropical cyclone (TC) ever observed in the Western Hemisphere (Kimber-
39 lain et al. 2016; Rogers et al. 2017). TCI dropsonde observations collected during this RI period
40 revealed dramatic changes in the cold-point tropopause height and upper-level static stability (Du-
41 ran and Molinari 2018). In particular, when Patricia was at tropical storm intensity shortly before
42 RI commenced, a strong inversion layer existed just above the cold-point tropopause. During the
43 first half of the RI period, this inversion layer weakened throughout Patricia’s inner core, with the
44 weakening most pronounced over the developing eye. By the time the storm reached its maximum
45 intensity of 95 m s^{-1} , the inversion layer over the eye had disappeared almost completely, which
46 was accompanied by a greater than 1-km increase in the tropopause height. Meanwhile over the
47 eyewall region, the static stability increased and the tropopause remained near its initial level.

48 Despite the importance of tropopause-layer thermodynamics in theoretical models of hurri-
49 canes (Emanuel and Rotunno 2011; Emanuel 2012), most observational studies of the upper-
50 tropospheric structure of TCs are decades old. Recently, however, Komaromi and Doyle (2017)
51 found that stronger TCs tended to have a higher and warmer tropopause over their inner core than
52 weaker TCs. Their results are consistent with the evolution observed over the inner core of Hur-

53 ricane Patricia, in which the tropopause height increased and the tropopause temperature warmed
54 throughout RI (Duran and Molinari 2018).

55 An idealized simulations of a TC analyzed by Ohno and Satoh (2015) suggested that the devel-
56 opment of an upper-level warm core near the 13-km level acted to decrease the static stability near
57 the tropopause within the eye. During the early stage of development in their simulation (their Fig.
58 9), static stability above 16 km was large at all radii. However, after the storm's intensification,
59 the static stability above 16 km within the eye was markedly smaller (their Fig. 10c). Although
60 the mechanisms that might drive this static stability evolution have not been examined explicitly
61 it might be related to the development of an upper-tropospheric warm care within the eye. Stern
62 and Zhang (2013) described the development of the TC warm core using a potential temperature
63 (θ) budget analysis. Although the warm anomaly in their simulation maximized in the mid-levels,
64 they also note that a secondary warming maximum existed in the 12-14-km layer. They found that
65 radial and vertical advection both played important roles in warm core development throughout
66 RI, and subgrid-scale diffusion became particularly important during the later stage of RI. The
67 warming of the upper troposphere by these advective and diffusive processes could contribute to
68 a decrease in static stability near the tropoopause within the eye. Other processes that can modify
69 the static stability in the upper troposphere of TCs include radiative heating within and near the
70 top of the cirrus canopy and shear-induced turbulent mixing near the outflow jet.

71 To our knowledge, the only paper that has examined explicitly the static stability evolution
72 in a modeled TC is Kepert et al. (2016), but their analysis was limited to the boundary layer.
73 The analysis herein is based upon that of Stern and Zhang (2013), except using a static stability
74 budget similar to that of Kepert et al. (2016), with a focus on the upper-tropospheric and lower-
75 stratospheric evolution during RI.

76 2. Model Setup

77 The numerical simulations were performed using version 19.4 of Cloud Model 1 (CM1) de-
78 scribed in Bryan and Rotunno (2009). The equations of motion were integrated on a 3000-km-
79 wide, 30-km-deep axisymmetric grid with 1-km horizontal and 250-m vertical grid spacing. The
80 computations were performed on an f -plane at 15°N latitude, over a sea surface with constant
81 temperature of 30.5°C, which matches that observed near Hurricane Patricia (2015; Kimberlain
82 et al. 2016). Horizontal turbulence was parameterized using the Smagorinsky scheme described
83 in Bryan and Rotunno (2009, pg. 1773), with a prescribed mixing length that varied linearly from
84 100 m at a surface pressure of 1015 hPa to 1000 m at a surface pressure of 900 hPa. Vertical
85 turbulence was parameterized using the formulation of Markowski and Bryan (2016, their Eq. 6),
86 using an asymptotic vertical mixing length of 100 m. A Rayleigh damping layer was applied out-
87 side of the 2900-km radius and above the 25-km level to prevent spurious gravity wave reflection
88 at the model boundaries. Microphysical processes were parameterized using the Thompson et al.
89 (2004) scheme and radiative heating tendencies were computed every two minutes using the Rapid
90 Radiative Transfer Model for GCMs (RRTMG) longwave and shortwave schemes (Iacono et al.
91 2008). The initial temperature and humidity field was horizontally homogeneous and determined
92 by averaging all Climate Forecast System Reanalysis (CFSR) grid points within 100 km of Pa-
93 tricia’s center of circulation at 18 UTC 21 October 2015. The vortex described in Rotunno and
94 Emanuel (1987, their Eq. 37) was used to initialize the wind field, setting all parameters equal to
95 the values used therein.

96 Although hurricanes simulated in an axisymmetric framework tend to be more intense than
97 those observed in nature, the intensity evolution of this simulation matches reasonably well with
98 that observed in Hurricane Patricia. After an initial spin-up period of about 20 hours, the modeled

storm (Fig. 1, blue lines) began an RI period that lasted approximately 30 hours. After this RI, the storm continued to intensify more slowly until the maximum 10-m wind speed reached 89 m s^{-1} and the sea-level pressure reached its minimum of 846 hPa 81 hours into the simulation. Hurricane Patricia (red stars) exhibited a similar intensity evolution prior to its landfall, with an RI period leading to a maximum 10-m wind speed of 95 m s^{-1} and a minimum sea-level pressure of 872 hPa.

3. Budget Computation

The static stability can be expressed as the squared Brunt-Väisälä frequency:

$$N_m^2 = \frac{g}{T} \left(\frac{\partial T}{\partial z} + \Gamma_m \right) \left(1 + \frac{T}{R_d/R_v + q_s} \frac{\partial q_s}{\partial T} \right) - \frac{g}{1 + q_t} \frac{\partial q_t}{\partial z}, \quad (1)$$

where g is gravitational acceleration, T is temperature, R_d and R_v are the gas constants of dry air and water vapor, respectively, q_s is the saturation mixing ratio, q_t is the total condensate mixing ratio, and Γ_m is the moist-adiabatic lapse rate:

$$\Gamma_m = g(1 + q_t) \left(\frac{1 + L_v q_s / R_d T}{c_{pm} + L_v \partial q_s / \partial T} \right), \quad (2)$$

where L_v is the latent heat of vaporization and c_{pm} is the specific heat of moist air at constant pressure. In the tropopause layer, q_s , $\partial q_s / \partial T$, and $\partial q_t / \partial z$ approach zero. In this limiting case, Eq. 1 reduces to:

$$N^2 = \frac{g}{\theta} \frac{\partial \theta}{\partial z}, \quad (3)$$

where θ is the potential temperature.

To compute N^2 , CM1 uses Eq. 1 in saturated environments and Eq. 3 in sub-saturated environments. For simplicity, however, only Eq. 3 will be employed for the budget computations throughout the entire domain¹.

¹The validity of this approximation will be substantiated later in this section.

Taking the time derivative of Eq. 3 yields the static stability tendency:

$$\frac{\partial N^2}{\partial t} = \frac{g}{\theta} \frac{\partial}{\partial z} \frac{\partial \theta}{\partial t} - \frac{g}{\theta^2} \frac{\partial \theta}{\partial z} \frac{\partial \theta}{\partial t}, \quad (4)$$

where the potential temperature tendency, $\partial \theta / \partial t$, can be written, following Bryan (cited 2018):

$$\frac{\partial \theta}{\partial t} = -u \frac{\partial \theta}{\partial r} - w \frac{\partial \theta}{\partial z} + HTURB + VTURB + MP + RAD + DISS \quad (5)$$

Each term on the right-hand side of Eq. 5 represents a θ budget variable, each of which is output directly by the model every minute.

The first term on the right-hand side of Eq. 4 is larger than the second term throughout most of the tropopause layer (not shown). Consequently, the contribution of each of the terms in Eq. 5 to the N^2 tendency can be interpreted in light of a vertical gradient of each term.

Taking the vertical gradient of the first two terms on the right-hand side of Eq. 5 yields the time tendency of the vertical θ gradient due to horizontal and vertical advection²:

$$\left(\frac{\partial}{\partial t} \frac{\partial \theta}{\partial z} \right)_{adv} = -u \frac{\partial}{\partial r} \frac{\partial \theta}{\partial z} - w \frac{\partial}{\partial z} \frac{\partial \theta}{\partial z} - \frac{\partial u}{\partial z} \frac{\partial \theta}{\partial r} - \frac{\partial w}{\partial z} \frac{\partial \theta}{\partial z}. \quad (6)$$

The first two terms on the right-hand side of Eq. 6 represent advection of static stability by the radial and vertical wind, respectively. These terms act to rearrange the static stability field, but cannot strengthen or weaken static stability maxima or minima. The third and fourth terms on the right-hand side of Eq. 6 represent, respectively, the tilting of isentropes in the presence of vertical wind shear, and the stretching or squashing of isentropes by vertical gradients of vertical velocity. Since these terms involve velocity gradients, they can act to strengthen or weaken static stability maxima or minima through differential advection. Unless otherwise stated, any reference to "advection" in this paper indicates the sum of all of the terms in Eq. 6.

²These terms include the tendencies due to implicit diffusion in the fifth-order finite differencing scheme, which are separated from the advection terms in the CM1 budget output

Returning to Eq. 5, HTURB and VTURB are the θ tendencies from the horizontal and vertical turbulence parameterizations, MP is the tendency from the microphysics scheme, RAD is the tendency from the radiation scheme, and DISS is the tendency due to turbulent dissipation. This equation neglects Rayleigh damping, since the entire analysis domain lies outside of the regions where damping is applied. Each term in Eq. 5 is substituted for $\partial\theta/\partial t$ in Eq. 4, yielding the contribution of each budget term to the static stability tendency. These terms are summed, yielding an instantaneous "budget change" in N^2 every minute. The budget changes are then averaged over 24-hour periods and compared to the total model change in N^2 over that same time period, i.e.:

$$\Delta N_{budget}^2 = \frac{1}{\delta t} \sum_{t=t_0}^{t_0+\delta t} \left. \frac{\partial N^2}{\partial t} \right|_t \quad (7)$$

$$\Delta N_{model}^2 = N_{t_0+\delta t}^2 - N_{t_0}^2 \quad (8)$$

$$Residual = \Delta N_{model}^2 - \Delta N_{budget}^2 \quad (9)$$

where t_0 is an initial time and δt is 24 hours.

Eqs. 7-9 are plotted for three consecutive 24-hour periods in Fig. 2. For this and all subsequent radial-vertical cross sections, a 1-2-1 smoother is applied once in the radial direction to eliminate $2\Delta r$ noise that appears in some of the raw model output and calculated fields. The left column of Fig. 2 depicts the model changes computed using Eq. 8, together with Eq. 1 in saturated environments and Eq. 3 in subsaturated environments. The center column depicts the budget changes computed using Eq. 7 together with Eq. 3 throughout the entire domain. Thus, the left column includes the effect of moisture in the N^2 computations, whereas the center column neglects moisture. The right column depicts the residuals, computed using Eq. 9 (i.e. the left column minus the center column.) In every 24-hour period, the budget changes are nearly identical to the model changes, which is reflected in the near-zero residuals in the right column. This indicates that the

154 budget accurately represents the model variability, which implies that the neglect of moisture in
155 the budget computation introduces negligible error within the analysis domain³.

156 In the tropopause layer, some of the budget terms are small enough to be ignored. To determine
157 which of the budget terms are most important, a time series of the contribution of each of the
158 budget terms in Eq. 5 to the tropopause-layer static stability tendency is plotted in Fig. 3. For this
159 figure, each of the budget terms is computed using the method described in Section 3, except with
160 1-hour averaging intervals instead of 24-hour intervals. The absolute values of these tendencies
161 are then averaged over the radius-height domain of the plots shown in Fig. 2 and plotted as a time
162 series⁴. Advection (Fig. 3, red line) plays an important role in the mean tropopause-layer static
163 stability tendency at all times, and vertical turbulence (Fig. 3, blue line) and radiation (Fig. 3, dark
164 green line) also contribute significantly. The remaining three processes - horizontal turbulence,
165 microphysics, and dissipative heating - are negligible everywhere outside of the eyewall, and do
166 not play important roles in the mesoscale tropopause variability.

167 The preceding analysis indicates that, at all times, three budget terms dominate the tropopause-
168 layer static stability tendency: advection, vertical turbulence, and radiation. Variations in the
169 magnitude and spatial structure of these terms drive the static stability changes depicted in Fig. 2;
170 subsequent sections will focus on these variations and what causes them.

³This is not the case in the lower- and mid-troposphere, where the residual actually exceeds the budget tendencies in many places, likely due to the neglect of moisture; thus we limit this analysis to the upper troposphere and lower stratosphere.

⁴It will be seen in subsequent figures that each of the terms contributes both positively and negatively to the N^2 tendency within the analysis domain. Thus, taking an average over the domain tends to wash out the positive and negative contributions. To circumvent this problem, the absolute value of each of the terms is averaged.

4. Results

a. Static stability evolution

The average N^2 over the first day of the simulation (Fig. 4a) indicates the presence of a weak N^2 maximum just above the cold-point tropopause. Over the subsequent 24 hours, during the RI period, the N^2 within and above this layer decreased within the 25-km radius (Fig. 4b). This decreasing N^2 corresponded to an increase in the tropopause height within the developing eye, maximized at the storm center. Outside of the eye, meanwhile, the tropopause height decreased over the eyewall region (25-60-km radius) and increased only slightly outside of the 60-km radius. In this outer region, the N^2 maximum just above the tropopause strengthened during RI. These trends continued as the storm's intensity leveled off in the 48-72-hour period (Fig. 4c). The tropopause height increased to nearly 21 km at the storm center and sloped sharply downward to 16.3 km on the inner edge of the eyewall, near the 30 km radius. Static stability outside of the eye, meanwhile, continued to increase just above the cold-point tropopause. This N^2 evolution closely follows that observed in Hurricane Patricia (2015; Duran and Molinari 2018, see their Fig. 4). The mechanisms that led to these N^2 changes will be investigated in the subsequent sections.

b. Static stability budget analysis

(i) 0-24 hours

The initial spin-up period was characterized by a steady increase of the maximum wind speed from 11 m s⁻¹ to 22 m s⁻¹ (Fig. 1a, blue line), an intensification rate that closely matched that of TC Patricia (Fig. 1a, red stars). The weakening of the lower-stratospheric static stability maximum during this period is reflected in the total N^2 budget change over this time (Fig. 5a). The layer just above the cold-point tropopause was characterized by decreasing N^2 (purple shading),

193 maximizing at the storm center. At and immediately below the tropopause, meanwhile, existed
 194 increasing N^2 during this time period. Although these tendencies extended out to the 200-km ra-
 195 dius, they were particularly pronounced at innermost radii. A comparison of the contributions of
 196 advection (Fig. 5b), vertical turbulence (Fig. 5c), and radiation (Fig. 5d) reveals that advection was
 197 the primary driver of the N^2 tendency during this period, acting to stabilize near and just below the
 198 tropopause and destabilize above. Although vertical turbulence acted in opposition to advection
 199 (i.e. it acted to stabilize regions that advection acted to destabilize), the magnitude of the advective
 200 tendencies was larger, particularly at the innermost radii. The sum of advection and vertical
 201 turbulence (Fig. 5e) almost exactly replicated the static stability tendencies above the tropopause.
 202 Radiative tendencies, meanwhile, (Fig. 5d) acted to destabilize the layer below about 16 km and
 203 stabilize the layer between 16 and 17 km. The sum of advection, vertical turbulence, and radiation
 204 (Fig. 5f) reproduced the total change in N^2 almost exactly.

205 (ii) 24-48 hours

206 During the RI period, the maximum wind speed increased from 22 m s^{-1} to 80 m s^{-1} . Over this
 207 time, N^2 within the eye generally decreased above 16 km and increased below (Fig. 6a), with the
 208 destabilization above 16 km maximizing near the level of the mean cold-point tropopause. These
 209 tendencies at the innermost radii were driven almost entirely by advection (Fig. 6b). Vertical
 210 turbulence (Fig. 6c) and radiation (Fig. 6d) contributed negligibly to the static stability tendencies
 211 in this region.

212 Outside of the eye, the N^2 evolution exhibited alternating layers of positive and negative tenden-
 213 cies. Near and above 18 km existed an upward-sloping region of decreasing N^2 that extended out
 214 to the 180-km radius. In this region, neither vertical turbulence nor radiation exhibited negative N^2
 215 tendencies; advection was the only forcing for this destabilization. Immediately below this layer,

216 just above the cold-point tropopause, was a region of increasing N^2 that sloped upward from 17
 217 km near the 30-km radius to just below 18 km outside of the 100-km radius. Advection and verti-
 218 cal turbulence both contributed to this positive N^2 tendency, with advection playing an important
 219 role below about 17.5 km and and turbulence playing an important role above. The sum of advec-
 220 tion and turbulence (Fig. 6e) reveals two separate regions of increasing N^2 in the 17-18-km layer
 221 rather than one contiguous region. The addition of radiation to these two terms, however, (Fig. 6f)
 222 provides the link between these two regions, indicating that radiation also plays a role in strength-
 223 ening the stable layer just above the tropopause. In the 16-17-km layer, just below the cold-point
 224 tropopause, a horizontally-extensive layer of destabilization also was forced by a combination of
 225 advection, vertical turbulence, and radiation. The sum of advection and vertical turbulence ac-
 226 counts for only a portion of the decreasing N^2 in this layer, and actually indicates forcing for
 227 stabilization near the 50-km radius and outside of the 130-km radius. Radiative tendencies over-
 228 come this forcing for stabilization in both of these regions to produce the radially-extensive region
 229 of destabilization observed just below the tropopause.

230 The sum of advection, vertical turbulence, and radiation (Fig. 6f) once again closely follows
 231 the observed N^2 variability, except in the eyewall region, where the neglect of latent heating and
 232 horizontal turbulence introduces some differences.

233 (iii) 48-72 hours

234 After the storm's maximum wind speed leveled off near 80 m s^{-1} , the magnitude of the static
 235 stability tendencies within the eye decreased to near zero (Fig. 7a).

236 Outside of the eye, however, N^2 continued to decrease in the layer immediately surrounding the
 237 tropopause. The sum of advection and vertical turbulence (Fig. 7e) indicates that the increase of
 238 N^2 observed in the 17-18-km layer and inside of the 80-km radius cannot be attributed to these

239 processes, since the sum of these two terms provided forcing for destabilization. Instead, radiation
 240 (Fig. 7d) provided the forcing for stabilization in this region. Outside of the 80-km radius, both
 241 advection (Fig. 7b) and vertical turbulence (Fig. 7c) provided forcing for stabilization near and
 242 just above the 18-km level. The sum of the two terms (Fig. 7e) indicates increasing N^2 near the
 243 18-km level everywhere outside of the 80-km radius, but this stabilization is slightly weaker in
 244 the 90-120-km radial band than the observed value. The addition of radiation (Fig. 7f) provided
 245 the extra forcing for stabilization required to account for the observed increase in N^2 . Outside
 246 of the 120-km radius, the region of radiative forcing for stabilization sloped downward, and the
 247 increase in N^2 observed near 18 km can be explained entirely by a combination of advection and
 248 vertical turbulence. The layer of decreasing N^2 observed near the tropopause was forced primarily
 249 by vertical turbulence and radiation. Within most of this region, advection provided strong forcing
 250 for stabilization, but this forcing was outweighed by the negative N^2 tendencies induced by a
 251 combination of vertical turbulence and radiation.

252 **5. Discussion**

253 *a. The role of advection*

254 Advection played an important role in the tropopause-layer N^2 evolution at all stages of intensifi-
 255 cation, but for brevity, this section will focus only on the RI (24-48-hour) period. To investigate the
 256 advective processes more closely, the individual contributions of horizontal and vertical advection
 257 during the RI period are shown in Fig. 8, along with the corresponding time-mean radial and verti-
 258 cal velocities and θ . The N^2 tendencies due to the two advective components (Fig. 8a,b) exhibited
 259 strong cancellation, consistent with flow that was nearly isentropic. There existed, however, a
 260 large region near the tropopause in which the total advective tendency was nonzero (Fig. 6b).

261 These nonzero tendencies were related to the development of the TC's secondary circulation as it
262 intensified.

263 During the RI period, strong radial and vertical circulations developed near the tropopause
264 (Fig. 8c,d), which forced high-magnitude N^2 tendencies due to advection (Fig. 8a,b). A layer
265 of strong outflow formed at and below the tropopause during this period, with the outflow maxi-
266 mum (dashed cyan line) curving from the 14-km level at the 50-km radius to just below the 16-km
267 level outside of the 80-km radius (Fig. 8c). Notably, the N^2 tendency due to horizontal advec-
268 tion (Fig. 8a) tended to switch signs at this line, with stabilization below the outflow maximum
269 and destabilization above. This is consistent with the outflow layer carrying air with increasingly
270 large θ from the eyewall to large radii as the storm intensified. This increase in θ maximized near
271 the outflow maximum, which acted to decrease $\partial\theta/\partial z$ above the outflow maximum and increase
272 it below. This mechanism is the same as that discussed in Trier and Sharman (2009), in which
273 vertical wind shear in the outflow layer of a mesoscale convective system acted to modify the
274 upper-tropospheric static stability through differential advection of isentropes.

275 Meanwhile in the lower stratosphere, a thin layer of 2-4 m s⁻¹ inflow developed a few hundred
276 meters above the tropopause, similar to that which was observed in Hurricane Patricia (2015;
277 Duran and Molinari 2018) and in previous modeling studies (e.g. Ohno and Satoh 2015; Kieu et al.
278 2016). Since the isentropes in this layer sloped slightly upward with radius (i.e. $\partial\theta/\partial r < 0$), this
279 inflow acted to import lower θ air from outer radii to inner radii. Since the negative θ tendencies
280 maximized at the level of maximum inflow, the layer below the inflow maximum destabilized and
281 the layer above stabilized (Fig. 8a).

282 Curiously, horizontal advection contributed to the N^2 tendency everywhere within the eye,
283 even though the mean radial velocity there was near zero. Close examination of the model out-
284 put revealed that these tendencies were forced by advective processes associated with inward-

285 propagating waves. Although the radial velocity perturbations induced by these waves averaged
286 out to zero, the advective tendencies forced by the radial velocity perturbations did not. Addition-
287 ally, when these waves reached $r=0$, a dipole of vertical velocity resulted, with ascent above and
288 descent below. For reasons that remain unclear, the regions of ascent were more persistent than the
289 regions of descent, which resulted in the mean ascent observed near $r=0$ above 17 km in Fig. 8b.

290 Vertical advection also played an important role in the tropopause-layer static stability evolution.
291 Within the eye, subsidence dominated below 17 km, while mean ascent existed near the storm
292 center above 17 km. Although the magnitude of the subsidence was larger at lower altitudes,
293 $\partial\theta/\partial z$ was smaller there. Because $\partial\theta/\partial z$ was smaller, the subsidence at lower levels could not
294 accomplish as much warming as the subsidence at higher levels in the eye, consistent with the
295 results of Stern and Zhang (2013). As a result, vertical advection within the eye acted to stabilize
296 the layer below 16 km during RI.

297 Outside of the 27-km radius, ascent dominated the troposphere, while a 1.5-km-deep layer of
298 descent existed immediately above the tropopause. These regions of ascent and descent converged
299 just above the tropopause; this convergence acted to compact the isentropes in this layer and in-
300 crease the static stability. Above the lower-stratospheric subsidence maximum, meanwhile, verti-
301 cal advection acted to decrease N^2 . Below the tropopause, differential vertical advection increased
302 N^2 within the eyewall region and also at larger radii above the vertical velocity maximum at larger
303 radii. Outside of the eyewall and below the vertical velocity maximum, meanwhile, differential
304 vertical advection acted to decrease N^2 .

305 Comparing the N^2 tendencies forced by horizontal (Fig. 8a) and vertical (Fig. 8b) advection
306 to the total advective tendency seen in Fig. 6b reveals that horizontal advective tendencies domi-
307 nated the troposphere, while vertical advective tendencies dominated the layer near and above the
308 tropopause. Thus, tilting of isentropes in the vicinity of the upper-tropospheric outflow maximum

appears to be the most important process governing the N^2 tendency in the troposphere, whereas convergence of vertical velocity appears to be the most important process near the tropopause.

b. The role of radiation

During the initial spin-up period (0-24 hours; Fig. 9a), convection was not deep enough to deposit large quantities of ice near the tropopause and create a persistent cirrus canopy. Due to the lack of ice particles, the radiative heating tendencies during this period (Fig. 9b) were relatively small and confined to the region above a few particularly strong, although transient, convective towers. During RI (24-48 hours), the eyewall updraft strengthened and a radially-extensive cirrus canopy developed near the tropopause (Fig. 9c). The enhanced vertical gradient of ice mixing ratio at the top of the cirrus canopy induced strong diurnal-mean radiative cooling near the tropopause (Fig. 9d). This cooling exceeded 0.6 K h^{-1} (14.4 K day^{-1}) in some places and sloped downward from the lower stratosphere into the upper troposphere, following the top of the cirrus canopy. A small radiative warming maximum also appeared outside of the 140-km radius below this region of cooling. These results broadly agree with those of Bu et al. (2014; see their Fig. 11a), whose CM1 simulations produced a 0.3 K h^{-1} diurnally-averaged radiative cooling at the top of the cirrus canopy and radiative warming within the cloud that maximized near the 200-km radius. This broad region of radiative cooling acted to destabilize the layer below the cooling maximum and stabilize the layer above, which can be seen in Fig. 6d. The small area of net radiative heating outside of the 140-km radius enhanced the destabilization above 16 km in this region and produced a thin layer of stabilization in the 15-16-km layer.

After the TC's RI period completed (48-72 hours), strong radiative cooling remained near the tropopause at inner radii (Fig. 9f), sloping downward with the top of the cirrus canopy to below the tropopause at outer radii. Cooling rates exceeded 1 K h^{-1} (24 K day^{-1}) just above the tropopause

332 between the 30- and 70-km radii. This value is more than three times the maximum cooling
333 rate of 0.3 K h^{-1} observed by Bu et al. (2014), a discrepancy that is a consequence of their larger
334 vertical grid spacing compared to that used here, along with a contribution from differing radiation
335 schemes. To compare our results to those of Bu et al. (2014), we ran a simulation identical to that
336 described in Section 2, except using the NASA-Goddard radiation scheme and 625-m vertical
337 grid spacing, to match those of Bu et al. (2014). This simulation produced a maximum 24-hour-
338 average radiative cooling rate of 0.3 K h^{-1} , which agrees with that shown in Bu et al. (2014).
339 Another simulation using 625-m vertical grid spacing and RRTMG radiation produced 24-hour-
340 average cooling rates of up to 0.6 K h^{-1} , which is consistent with the WRF simulations of Bu et al.
341 (2014). This suggests that vertical grid spacing smaller than 625 m is necessary to resolve properly
342 the radiative cooling at the top of the cirrus canopy, and that the results can be quite sensitive to
343 the radiation scheme used.

344 Meanwhile below the tropopause, time-mean radiative warming spread from 30- to 160-km
345 radius within the cirrus canopy. The existence of radiative cooling overlying radiative warming in
346 this region led to radiatively-forced destabilization at and below the tropopause, as was observed
347 in Fig. 7d. Beneath the warming layer existed a region of forcing for stabilization, while a much
348 stronger region of forcing for stabilization existed in the lower stratosphere, above the cooling
349 maximum.

350 The results herein suggest that radiative heating tendencies played an important role in destabi-
351 lizing the upper troposphere and stabilizing the lower stratosphere after the cirrus canopy devel-
352 oped.

353 *c. The role of turbulent mixing*

354 Fig. 10 depicts the effect of turbulent mixing on the θ profile of an initially stably-stratified
355 layer. At the initial time in this idealized case, θ increases with height at a constant rate (Fig. 10,
356 left panel). The imposition of turbulence (blue hatching) adjusts the θ profile within the mixed
357 layer toward a constant value equal to the mean value of that layer in the initial state (Fig. 10, right
358 panel). Just above and just below the mixed layer, however, the θ profile remains undisturbed.
359 Consequently, although turbulent mixing acts to decrease $\partial\theta/\partial z$ in the layer in which it is occur-
360 ring, it actually increases $\partial\theta/\partial z$ just below and just above the layer. These vertical gradients of
361 turbulent mixing are quite important, particularly on the flanks of the upper-tropospheric outflow
362 jet.

363 Two distinct maxima of vertical eddy diffusivity developed in the tropopause layer as the storm
364 intensified (Fig. 11). Comparison of these turbulent regions to the N^2 tendencies in Figs. 6c and
365 7c reveals that the layers in which vertical eddy diffusivity maximized corresponded to layers of
366 destabilization due to vertical turbulence. Just outside of these layers, however, vertical turbulence
367 acted to increase N^2 . The large vertical gradient of vertical eddy diffusivity near the tropopause
368 played an important role in developing the lower-stratospheric stable layer during RI. This supports
369 the hypothesized role of turbulence in setting the outflow-layer θ stratification in Rotunno and
370 Emanuel (1987).

371 **6. Conclusions**

372 The simulated N^2 evolution shown herein closely matched that observed during the RI of Hur-
373 ricane Patricia (2015). Three processes dominated the N^2 variability in the upper troposphere and
374 lower stratosphere: advection, radiation, and vertical turbulence. Radiation and vertical turbulence

375 played particularly important roles in developing the strong N^2 maximum just above the cold-point
376 tropopause during RI.

377 To put the N^2 variability observed near the tropopause into context, Fig. 12 depicts the model
378 change in N^2 over the RI period from 0 to 21 km altitude, along with the vertical eddy diffusivity
379 and the radiative heating rate. It is clear that the largest changes in N^2 occurred in a relatively
380 shallow layer immediately surrounding the tropopause (Fig. 12a). This shallow layer also con-
381 tained the largest diurnally-averaged radiative heating tendencies found anywhere in the domain
382 (Fig. 12c). Values of vertical eddy diffusivity larger than any found outside of the boundary layer
383 also resided in the upper troposphere (Fig. 12b). The results herein suggest that this turbulence
384 not only develops as a response to the presence of small static stability and large vertical wind
385 shear, as discussed by Molinari et al. (2014) and Duran and Molinari (2016), but also can actively
386 increase the static stability in highly localized regions just above and below the mixed layers.

387 Since two of the most important processes contributing to the N^2 variability are parameter-
388 ized, and one (radiation) closely depends on yet another parameterized process (microphysics),
389 the tropopause-layer N^2 variability could be quite sensitive to the assumptions inherent to the pa-
390 rameterizations used. A better understanding of the microphysical characteristics of the TC cirrus
391 canopy, its interaction with radiation, and outflow-layer turbulence is critical to understanding the
392 tropopause-layer N^2 evolution.

393 In this paper, all of the variables were averaged over a full diurnal cycle to eliminate the effects
394 of diurnal variability and isolate the overall storm evolution. Diurnal variations in static stability
395 near the tropopause are potentially of interest with respect to the tropical cyclone diurnal cycle,
396 and will be the subject of future work.

397 *Acknowledgments.* We are indebted to George Bryan for his continued development and support
398 of Cloud Model 1. We also thank Jeffrey Kepert, Robert Fovell, and Erika Navarro for helpful
399 conversations related to this work. This research was supported by NSF Grant #1636799.

400 **References**

- 401 Bryan, G. H., 2012: Effects of surface exchange coefficients and turbulence length scales on the
402 intensity and structure of numerically simulated hurricanes. *Mon. Wea. Rev.*, **140**, 1125–1143.
- 403 Bryan, G. H., cited 2018: The governing equations for CM1. [Available online at http://www2.mmm.ucar.edu/people/bryan/cm1/cm1_equations.pdf].
- 405 Bryan, G. H., and R. Rotunno, 2009: The maximum intensity of tropical cyclones in axisymmetric
406 numerical model simulations. *Mon. Wea. Rev.*, **137**, 1770–1789.
- 407 Bu, Y. P., R. G. Fovell, and K. L. Corbosiero, 2014: Influence of cloud-radiative forcing on tropical
408 cyclone structure. *J. Atmos. Sci.*, **71**, 1644–1622.
- 409 Doyle, J. D., and Coauthors, 2017: A view of tropical cyclones from above: The Tropical Cyclone
410 Intensity (TCI) Experiment. *Bull. Amer. Meteor. Soc.*, **98**, 2113–2134.
- 411 Duran, P., and J. Molinari, 2016: Upper-tropospheric low Richardson number in tropical cyclones:
412 Sensitivity to cyclone intensity and the diurnal cycle. *J. Atmos. Sci.*, **73**, 545–554.
- 413 Duran, P., and J. Molinari, 2018: Dramatic inner-core tropopause variability during the rapid
414 intensification of Hurricane Patricia (2015). *Mon. Wea. Rev.*, **146**, 119–134.
- 415 Emanuel, K., 2012: Self-stratification of tropical cyclone outflow. Part II: Implications for storm
416 intensification. *J. Atmos. Sci.*, **69**, 988–996.

417 Emanuel, K., and R. Rotunno, 2011: Self-stratification of tropical cyclone outflow. Part I: Impli-
 418 cations for storm structure. *J. Atmos. Sci.*, **68**, 2236–2249.

419 Iacono, M. J., J. S. Delamere, E. J. Mlawer, M. W. Shephard, S. A. Clough, and W. D. Collins,
 420 2008: Radiative forcing by long-lived greenhouse gases: Calculations with the AER radiative
 421 transfer models. *J. Geophys. Res.*, **113** (D13103).

422 Kepert, J. D., J. Schwendike, and H. Ramsay, 2016: Why is the tropical cyclone boundary layer
 423 not "well mixed"? *J. Atmos. Sci.*, **73**, 957–973.

424 Kieu, C., V. Tallapragada, D.-L. Zhang, and Z. Moon, 2016: On the development of double warm-
 425 core structures in intense tropical cyclones. *J. Atmos. Sci.*, **73**, 4487–4506.

426 Kimberlain, T. B., E. S. Blake, and J. P. Cangialosi, 2016: Tropical cyclone report: Hurricane
 427 Patricia. National Hurricane Center. [Available online at www.nhc.noaa.gov].

428 Komaromi, W. A., and J. D. Doyle, 2017: Tropical cyclone outflow and warm core structure as
 429 revealed by HS3 dropsonde data. *Mon. Wea. Rev.*, **145**, 1339–1359.

430 Markowski, P. M., and G. H. Bryan, 2016: LES of laminar flow in the PBL: A potential problem
 431 for convective storm simulations. *Mon. Wea. Rev.*, **144**, 1841–1850.

432 Molinari, J., P. Duran, and D. Vollaro, 2014: Low Richardson number in the tropical cyclone
 433 outflow layer. *J. Atmos. Sci.*, **71**, 3164–3179.

434 Ohno, T., and M. Satoh, 2015: On the warm core of a tropical cyclone formed near the tropopause.
 435 *J. Atmos. Sci.*, **72**, 551–571.

436 Rogers, R. F., S. Aberson, M. M. Bell, D. J. Cecil, J. D. Doyle, J. Morgerman, L. K. Shay, and
 437 C. Velden, 2017: Re-writing the tropical record books: The extraordinary intensification of
 438 Hurricane Patricia (2015). *Bull. Amer. Meteor. Soc.*, **98**, 2091–2112.

439 Rotunno, R., and K. A. Emanuel, 1987: An air-sea interaction theory for tropical cyclones. Part II:
440 Evolutionary study using a nonhydrostatic axisymmetric numerical model. *J. Atmos. Sci.*, **44**,
441 542–561.

442 Stern, D. P., and F. Zhang, 2013: How does the eye warm? Part I: A potential temperature budget
443 analysis of an idealized tropical cyclone. *J. Atmos. Sci.*, **70**, 73–89.

444 Thompson, G., R. M. Rasmussen, and K. Manning, 2004: Explicit forecasts of winter precipitation
445 using an improved bulk microphysics scheme. Part I: Description and sensitivity analysis. *Mon.*
446 *Wea. Rev.*, **132**, 519–542.

447 Trier, S. B., and R. D. Sharman, 2009: Convection-permitting simulations of the environment sup-
448 porting widespread turbulence within the upper-level outflow of a mesoscale convective system.
449 *Mon. Wea. Rev.*, **137**, 1972–1990.

LIST OF FIGURES

- Fig. 1.** The maximum 10-m wind speed (top panel; m s^{-1}) and minimum sea-level pressure (bottom panel; hPa) in the simulated storm (blue lines; plotted every minute) and from Hurricane Patricia's best track (red stars; plotted every six hours beginning at the time Patricia attained tropical storm intensity). The rapid weakening during the later stage of Patricia's lifetime was induced by landfall. 26
- Fig. 2.** Left panels: Twenty-four-hour changes in squared Brunt-Väisälä frequency (N^2 ; 10^{-4} s^{-2}) computed using Eq. 8 over (top row) 0-24 hours, (middle row) 24-48 hours, (bottom row) 48-72 hours. Middle Panels: The N^2 change over the same time periods computed using Eqs. 4-7, Right Panels: The budget residual over the same time periods, computed by subtracting the budget change (middle column) from the model change (left column). Orange lines represent the cold-point tropopause height averaged over the same time periods. 27
- Fig. 3.** Time series of the contribution of each of the budget terms to the time tendency of the squared Brunt-Väisälä frequency (N^2 ; 10^{-4} s^{-2}). For each budget term, the absolute value of the N^2 tendency is averaged temporally over 1-hour periods (using output every minute), and spatially in a region extending from 0 to 200 km radius and 14 to 21 km altitude. 28
- Fig. 4.** Twenty-four-hour averages of squared Brunt-Väisälä frequency (N^2 ; 10^{-4} s^{-2}) over (a) 0-24 hours, (b) 24-48 hours, (c) 48-72 hours. Orange lines represent the cold-point tropopause height averaged over the same time periods. 29
- Fig. 5.** (a) Total change in N^2 over the 0-24-hour period ($10^{-4} \text{ s}^{-2} (24 \text{ h})^{-1}$) and the contributions to that change from (b) the sum of horizontal and vertical advection, (c) vertical turbulence, (d) longwave and shortwave radiation, (e) the sum of horizontal advection, vertical advection, and vertical turbulence, and (f) the sum of horizontal advection, vertical advection, vertical turbulence, and longwave and shortwave radiation. Orange lines represent the cold-point tropopause height averaged over the 0-24-hour period. 31
- Fig. 6.** As in Fig. 5, but for the 24-48-hour period. 32
- Fig. 7.** As in Fig. 5, but for the 48-72-hour period. 33
- Fig. 8.** The contributions to the change in N^2 over the 24-48-hour period ($10^{-4} \text{ s}^{-2} (24 \text{ h})^{-1}$) by (a) horizontal advection and (b) vertical advection. (c) The radial velocity (m s^{-1} ; filled contours), potential temperature (K; thick black contours), cold-point tropopause height (orange line), and level of maximum outflow (dashed cyan line) averaged over the 24-48-hour period. (d) The vertical velocity (cm s^{-1} ; filled contours), potential temperature (K; thick black contours), and cold-point tropopause height (orange line) averaged over the 24-48-hour period. 34
- Fig. 9.** Ice mixing ratio (g kg^{-1}) and cold-point tropopause height (orange lines) averaged over (a) 0-24 hours, (c) 24-48 hours, and (e) 48-72 hours. Radiative heating rate (K h^{-1}) and cold-point tropopause height (orange lines) averaged over (b) 0-24 hours, (d) 24-48 hours, and (f) 48-72 hours. 36
- Fig. 10.** Idealized schematic diagram of turbulent mixing in a stably-stratified layer. At the initial time (left panel), potential temperature increases with height at a constant rate (thick black line). The imposition of turbulence within a portion of the layer (blue hatching) adjusts the potential temperature profile toward the mean initial value of that layer. After a period of

492	mixing (right panel) the potential temperature in the mixed layer does not vary with height,	
493	but just above and just below the mixed layer, it rapidly increases with height.	37
494	Fig. 11. Vertical eddy diffusivity ($\text{m}^2 \text{s}^{-2}$; filled contours), cold-point tropopause height (cyan lines),	
495	and radial velocity (m s^{-1} ; thick black lines) averaged over (a) 0-24 hours, (b) 24-48 hours,	
496	and (c) 48-72 hours.	38
497	Fig. 12. (Top panel) Change in N^2 over the 24-48-hour period ($10^{-4} \text{s}^{-2} (24 \text{ h})^{-1}$) directly output by	
498	the model for the 0-21-km layer. (Middle panel) Vertical eddy diffusivity ($\text{m}^2 \text{s}^{-2}$) averaged	
499	over the same time period. (Bottom panel) Radiative heating rate (K h^{-1}) averaged over the	
500	same time period.	40

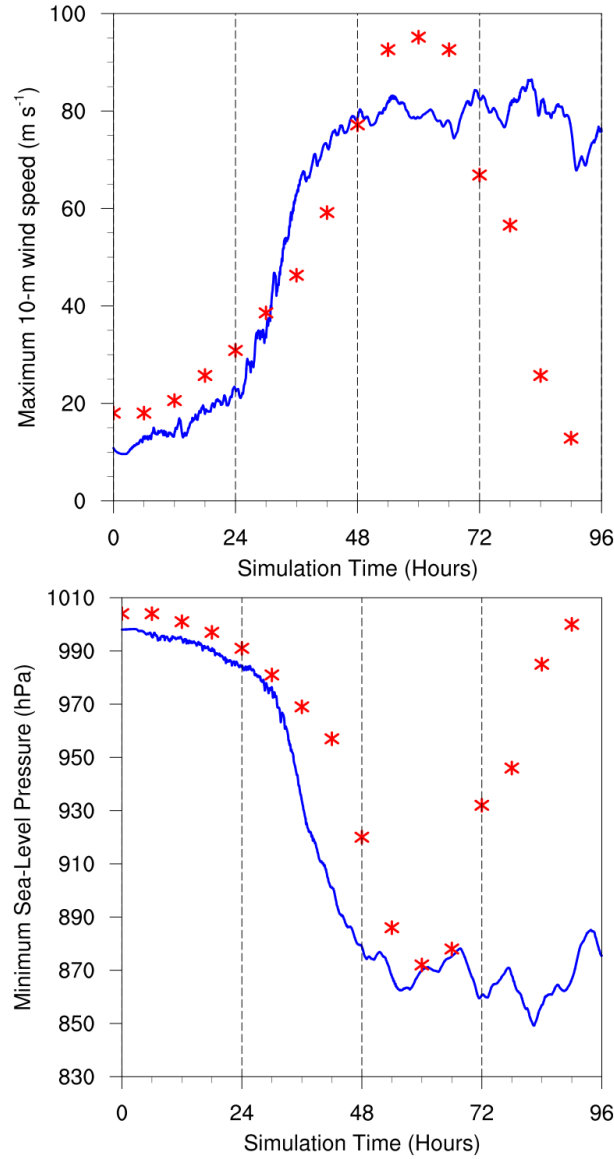


FIG. 1. The maximum 10-m wind speed (top panel; m s^{-1}) and minimum sea-level pressure (bottom panel; hPa) in the simulated storm (blue lines; plotted every minute) and from Hurricane Patricia's best track (red stars; plotted every six hours beginning at the time Patricia attained tropical storm intensity). The rapid weakening during the later stage of Patricia's lifetime was induced by landfall.

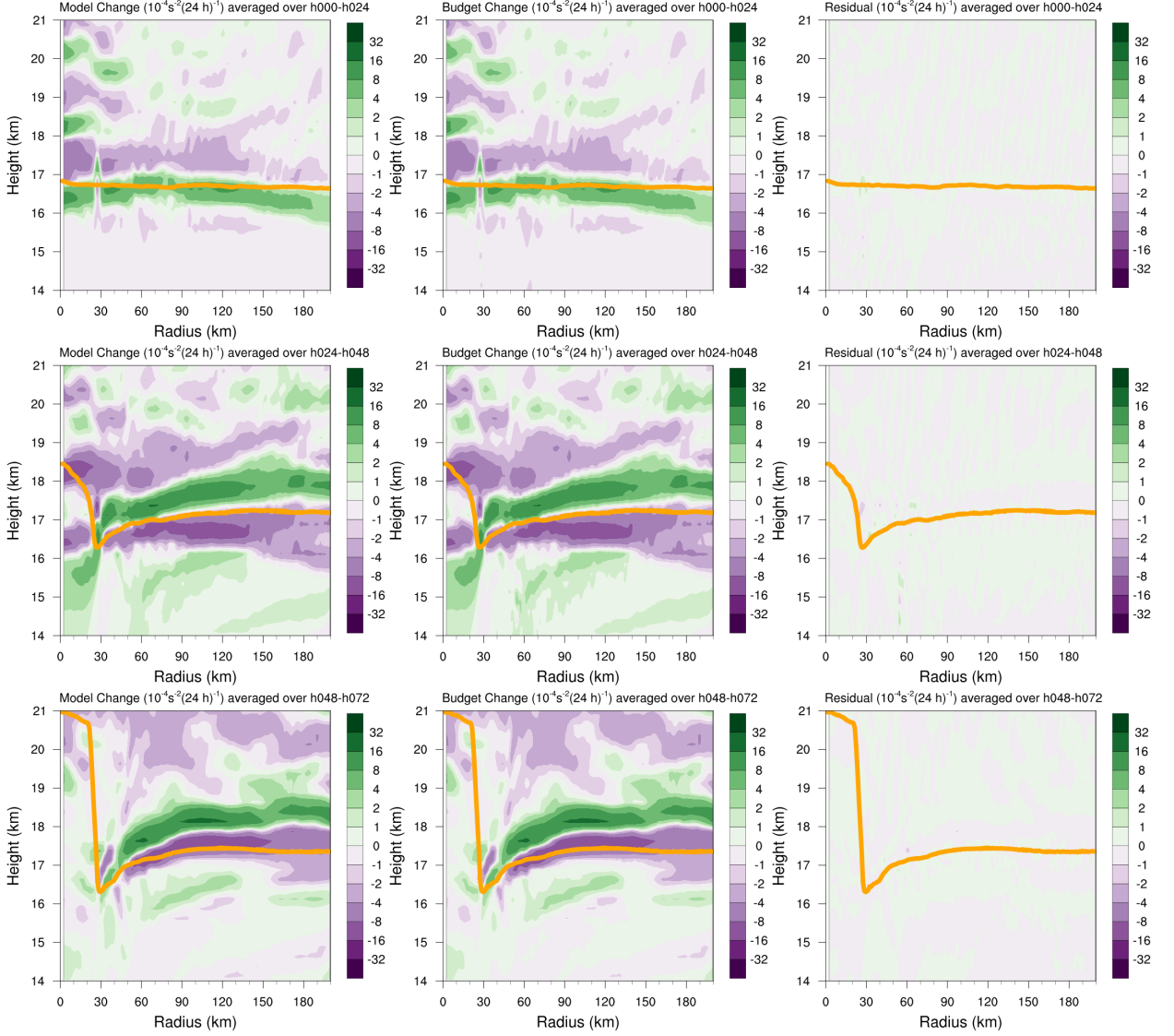


FIG. 2. Left panels: Twenty-four-hour changes in squared Brunt-Väisälä frequency (N^2 ; 10^{-4} s^{-2}) computed using Eq. 8 over (top row) 0-24 hours, (middle row) 24-48 hours, (bottom row) 48-72 hours. Middle Panels: The N^2 change over the same time periods computed using Eqs. 4-7, Right Panels: The budget residual over the same time periods, computed by subtracting the budget change (middle column) from the model change (left column). Orange lines represent the cold-point tropopause height averaged over the same time periods.

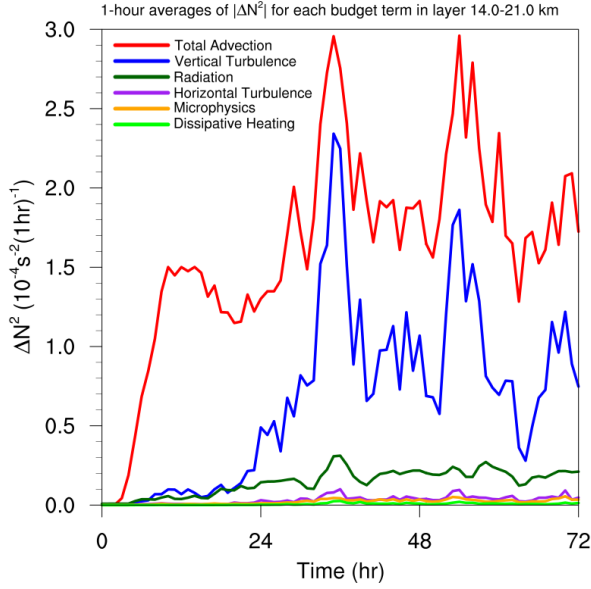


FIG. 3. Time series of the contribution of each of the budget terms to the time tendency of the squared Brunt-Väisälä frequency (N^2 ; 10^{-4} s^{-2}). For each budget term, the absolute value of the N^2 tendency is averaged temporally over 1-hour periods (using output every minute), and spatially in a region extending from 0 to 200 km radius and 14 to 21 km altitude.

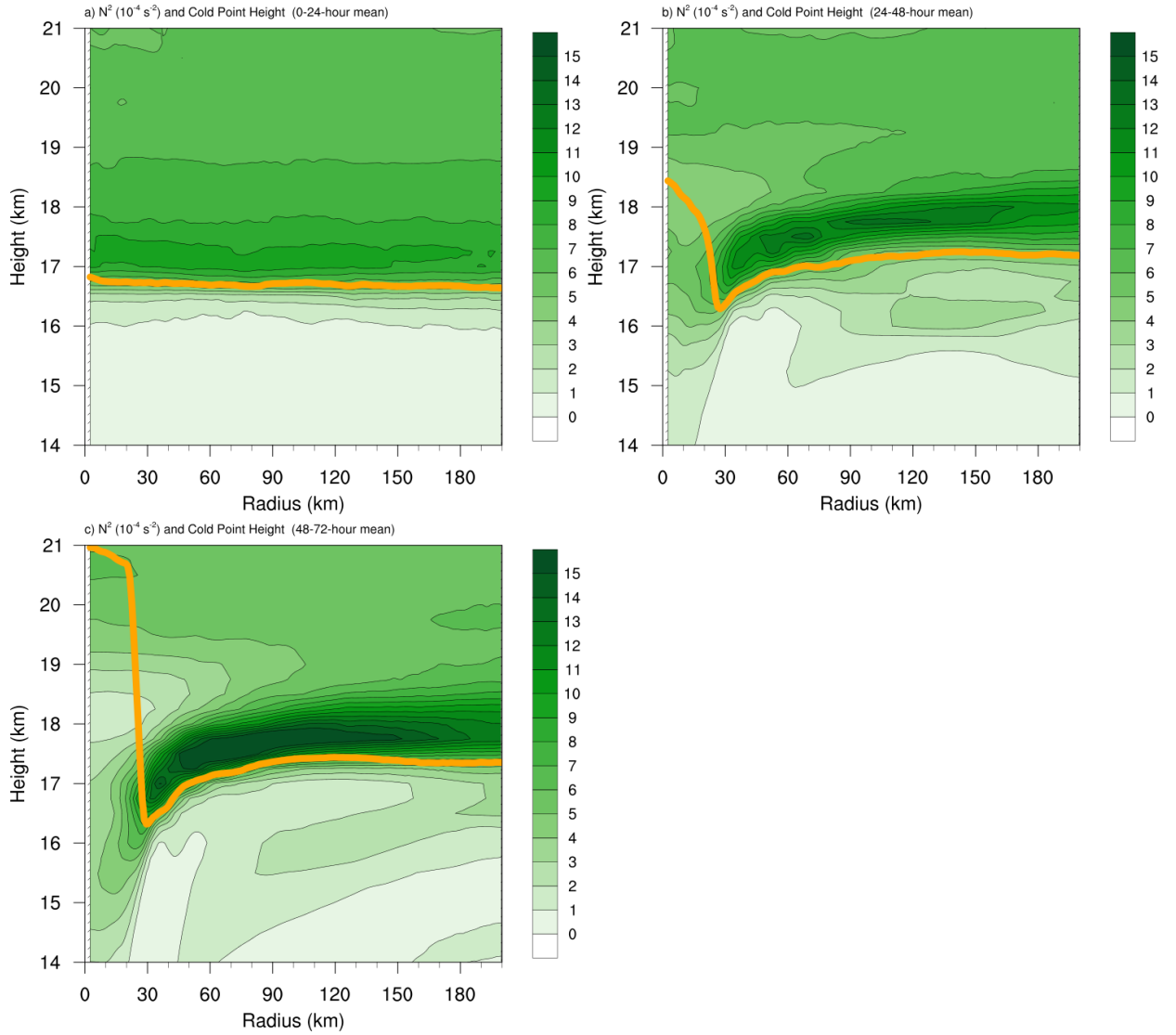
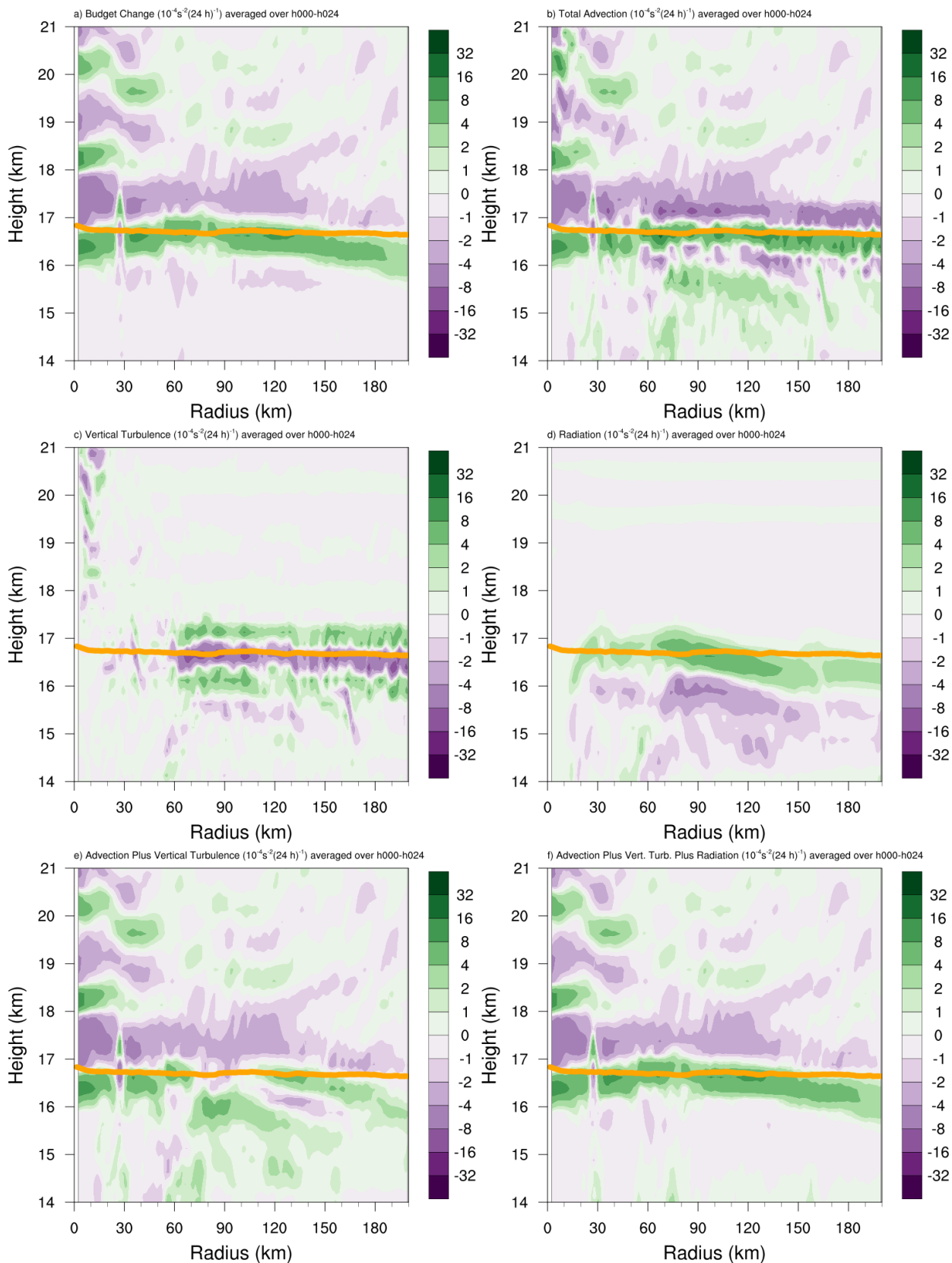


FIG. 4. Twenty-four-hour averages of squared Brunt-Väisälä frequency (N^2 ; 10^{-4} s^{-2}) over (a) 0-24 hours, (b) 24-48 hours, (c) 48-72 hours. Orange lines represent the cold-point tropopause height averaged over the same time periods.



517 FIG. 5. (a) Total change in N^2 over the 0-24-hour period ($10^{-4} \text{ s}^{-2} (24 \text{ h})^{-1}$) and the contributions to that change
518 from (b) the sum of horizontal and vertical advection, (c) vertical turbulence, (d) longwave and shortwave
519 radiation, (e) the sum of horizontal advection, vertical advection, and vertical turbulence, and (f) the sum of
520 horizontal advection, vertical advection, vertical turbulence, and longwave and shortwave radiation. Orange
521 lines represent the cold-point tropopause height averaged over the 0-24-hour period.

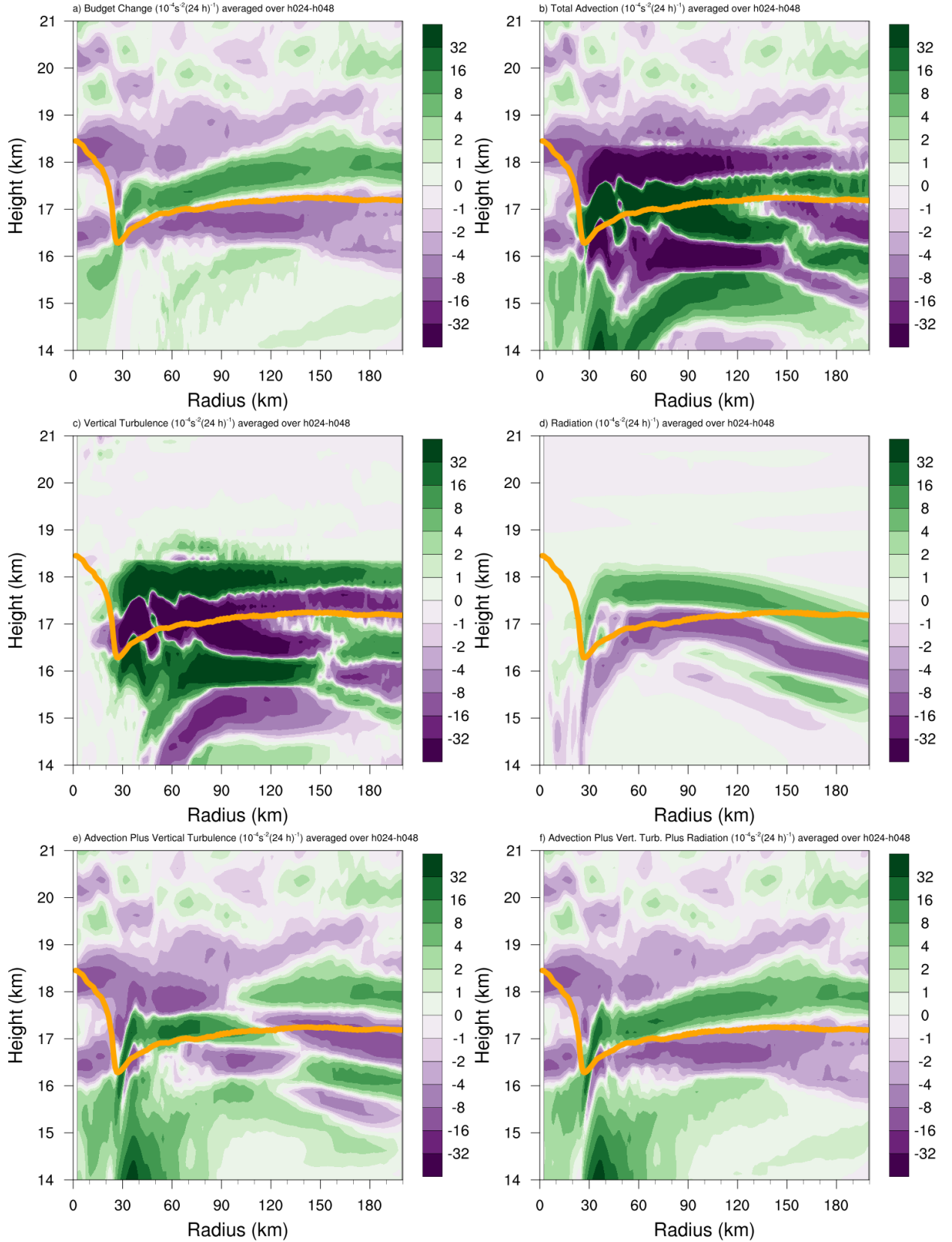


FIG. 6. As in Fig. 5, but for the 24-48-hour period.

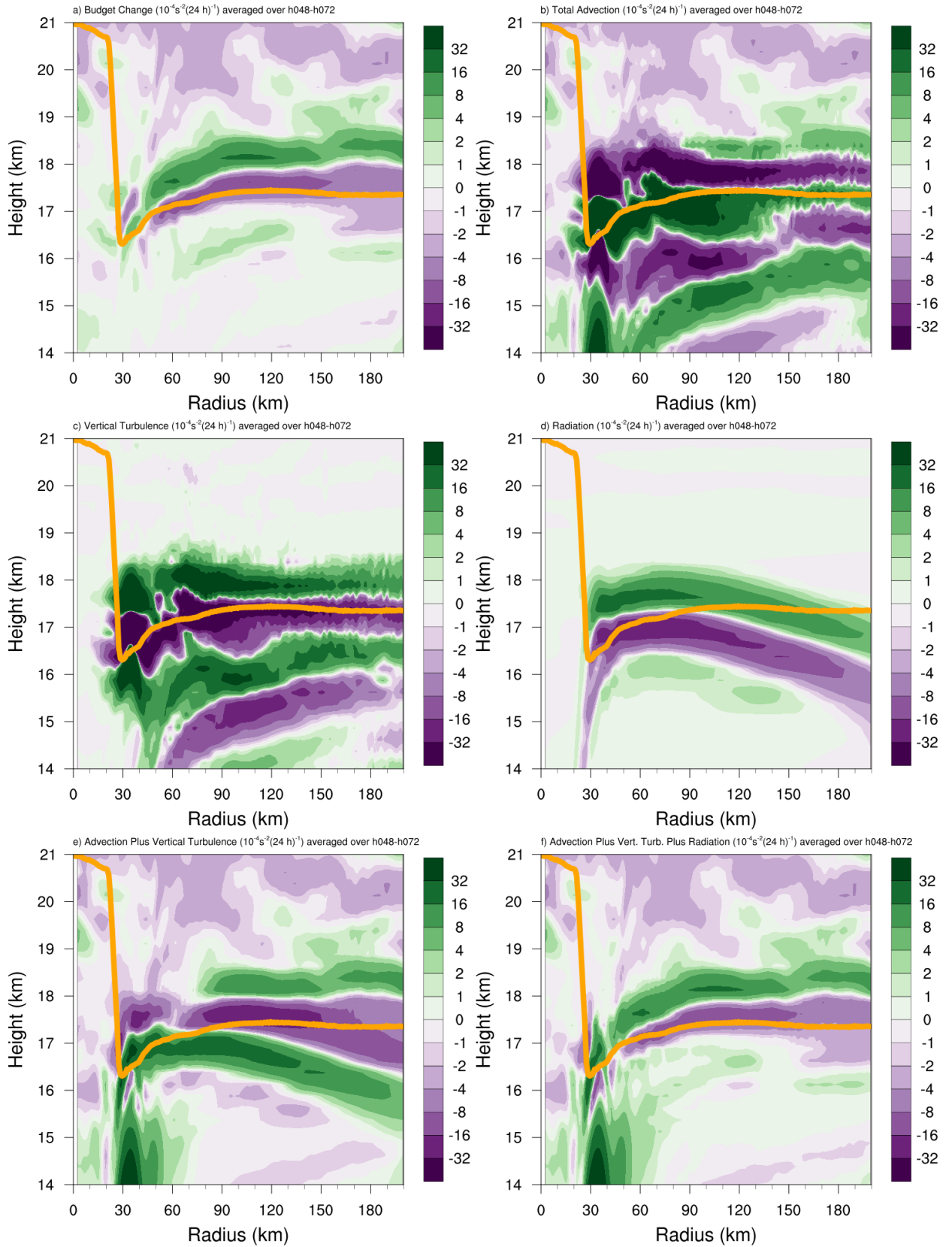


FIG. 7. As in Fig. 5, but for the 48-72-hour period.

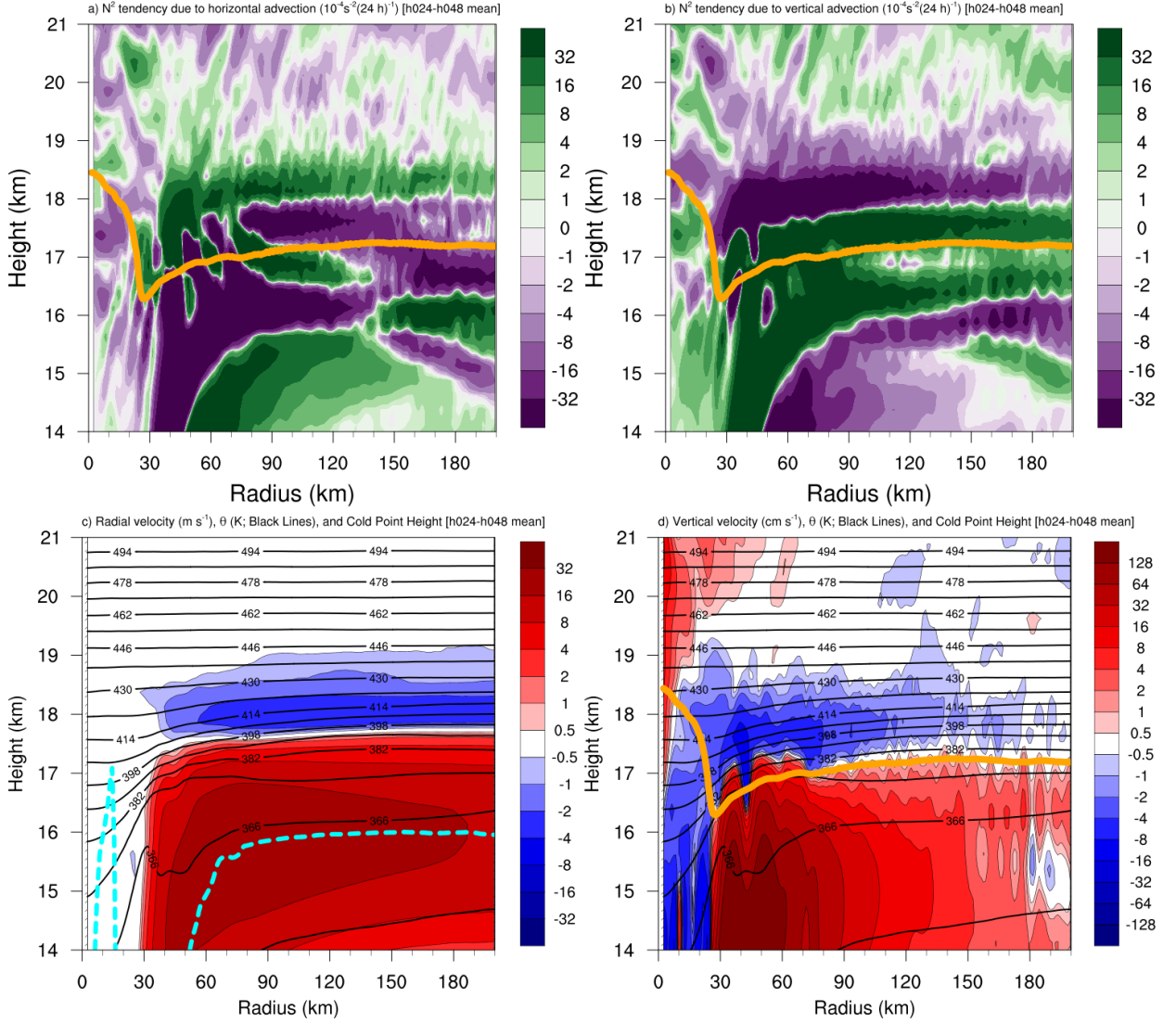
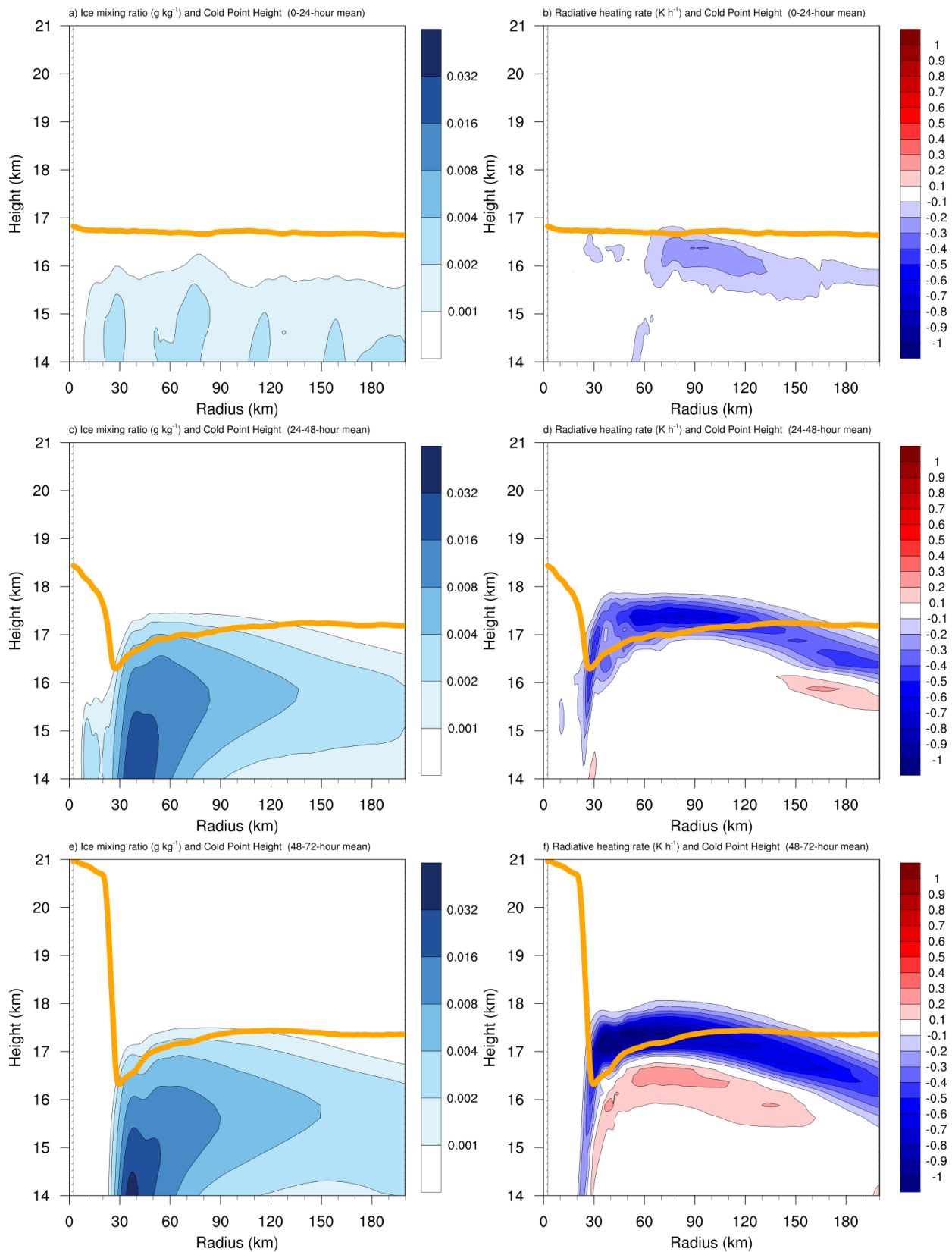


FIG. 8. The contributions to the change in N^2 over the 24-48-hour period ($10^{-4} \text{ s}^{-2} (24 \text{ h})^{-1}$) by (a) horizontal advection and (b) vertical advection. (c) The radial velocity (m s^{-1} ; filled contours), potential temperature (K; thick black contours), cold-point tropopause height (orange line), and level of maximum outflow (dashed cyan line) averaged over the 24-48-hour period. (d) The vertical velocity (cm s^{-1} ; filled contours), potential temperature (K; thick black contours), and cold-point tropopause height (orange line) averaged over the 24-48-hour period.



528 FIG. 9. Ice mixing ratio (g kg^{-1}) and cold-point tropopause height (orange lines) averaged over (a) 0-24 hours,
529 (c) 24-48 hours, and (e) 48-72 hours. Radiative heating rate (K h^{-1}) and cold-point tropopause height (orange
530 lines) averaged over (b) 0-24 hours, (d) 24-48 hours, and (f) 48-72 hours.

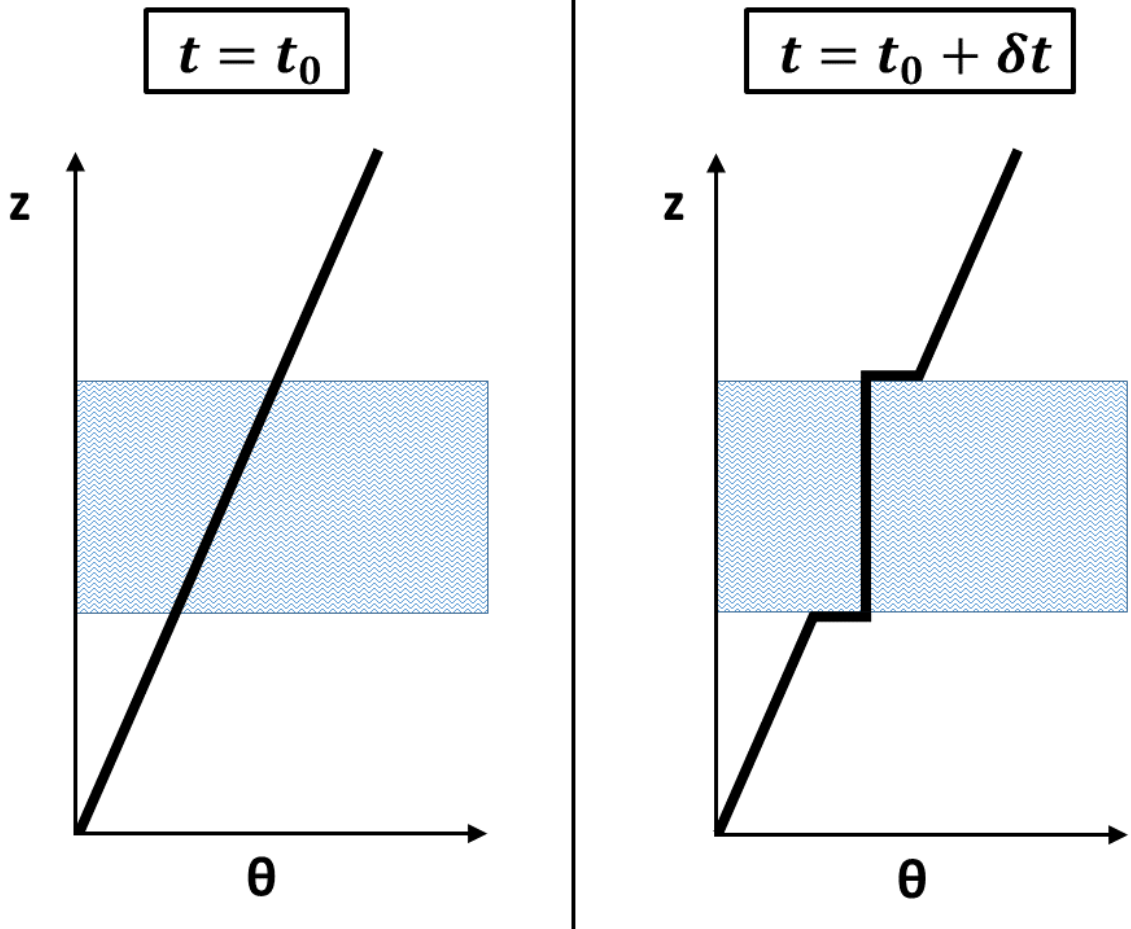


FIG. 10. Idealized schematic diagram of turbulent mixing in a stably-stratified layer. At the initial time (left panel), potential temperature increases with height at a constant rate (thick black line). The imposition of turbulence within a portion of the layer (blue hatching) adjusts the potential temperature profile toward the mean initial value of that layer. After a period of mixing (right panel) the potential temperature in the mixed layer does not vary with height, but just above and just below the mixed layer, it rapidly increases with height.

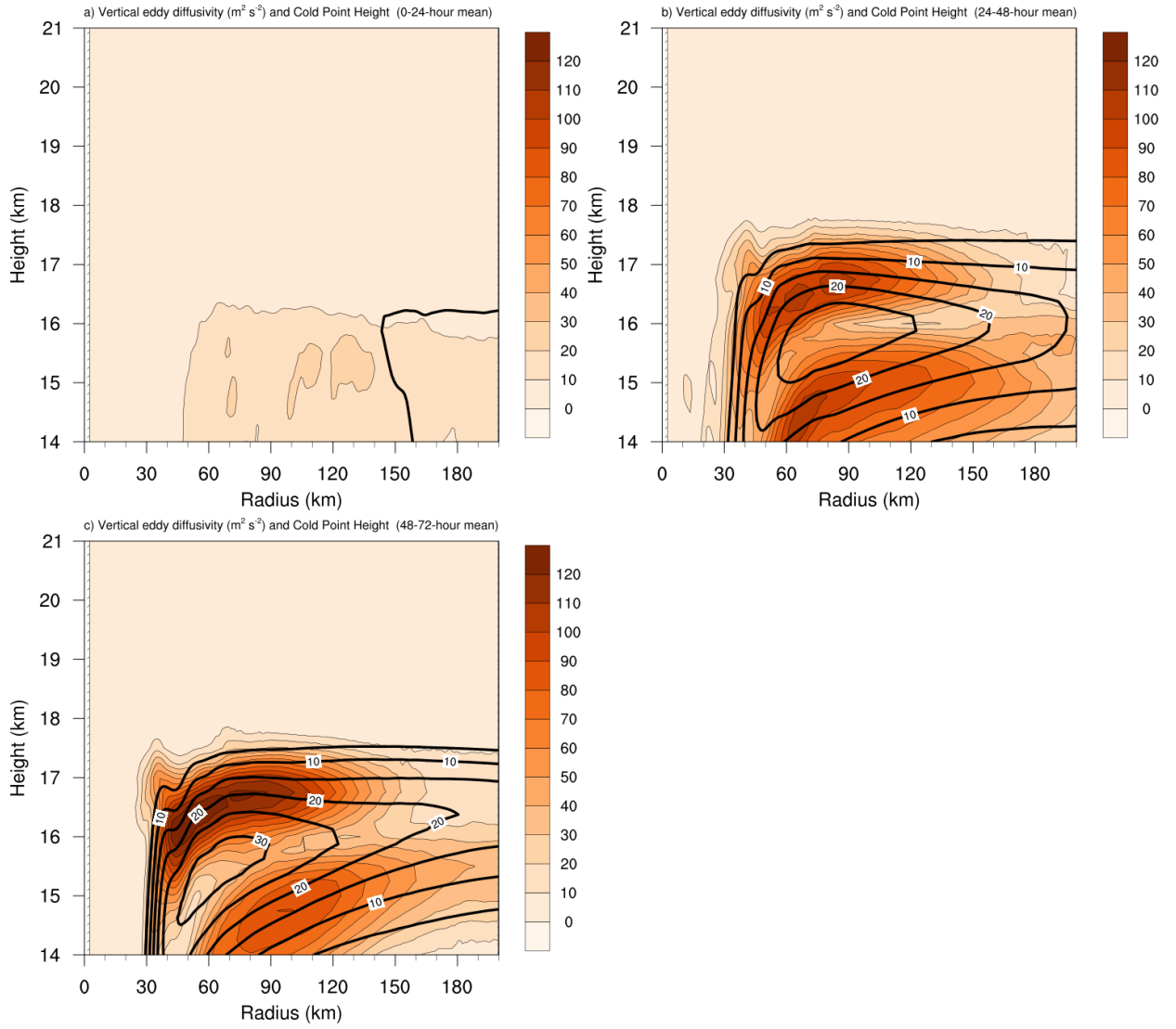
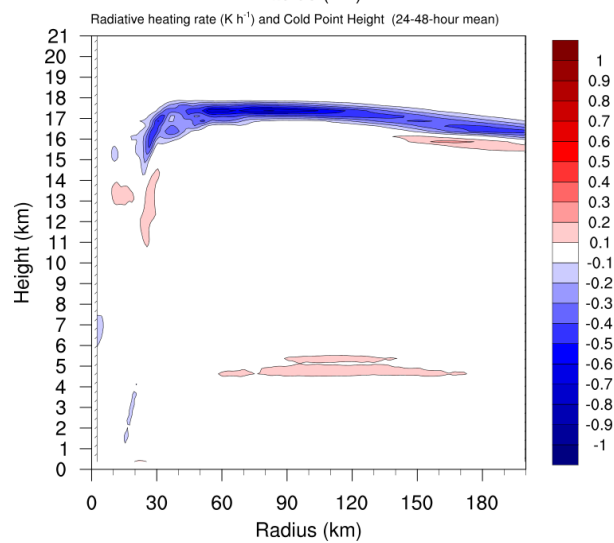
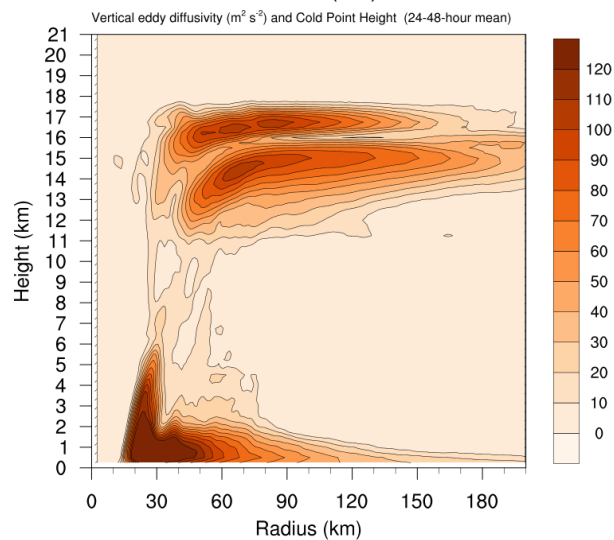
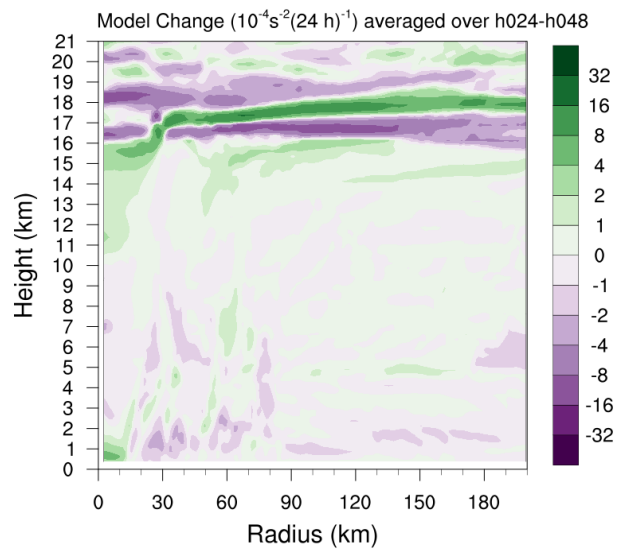


FIG. 11. Vertical eddy diffusivity ($\text{m}^2 \text{s}^{-2}$; filled contours), cold-point tropopause height (cyan lines), and radial velocity (m s^{-1} ; thick black lines) averaged over (a) 0-24 hours, (b) 24-48 hours, and (c) 48-72 hours.



538 FIG. 12. (Top panel) Change in N^2 over the 24-48-hour period ($10^{-4} \text{ s}^{-2} (24 \text{ h})^{-1}$) directly output by the model
539 for the 0-21-km layer. (Middle panel) Vertical eddy diffusivity ($\text{m}^2 \text{ s}^{-2}$) averaged over the same time period.
540 (Bottom panel) Radiative heating rate (K h^{-1}) averaged over the same time period.